Title
Antigorite crystallographic preferred orientations in serpentinites from Japan

Authors
Soda, Yusuke
Wenk, Hans-Rudolf

Publication Date
2014-03-01

DOI
10.1016/j.tecto.2013.12.016

Peer reviewed

Tectonophysics 615–616 (2014) 199–212

Contents lists available at ScienceDirect

Tectonophysics

journal homepage: www.elsevier.com/locate/tecto

Antigorite crystallographic preferred orientations in serpentinites from Japan

Yusuke Soda [a,*], Hans-Rudolf Wenk [b]

[a] School of Natural System, College of Science and Engineering, Kanazawa University, Kakuma-machi, Kanazawa 920-1192, Japan
[b] Department of Earth and Planetary Science, University of California, Berkeley, CA 94720, USA

ARTICLE INFO

Article history:
Received 16 November 2013
Received in revised form 14 December 2013
Accepted 23 December 2013
Available online 31 December 2013

Keywords:
Antigorite
Serpentinite
Crystallographic preferred orientation (CPO)
Seismic anisotropy
EBSD
Synchrotron X-ray

ABSTRACT

Foliated antigorite serpentinites are contributing to seismic anisotropy in subduction zones. However, uncertainty remains regarding the development of antigorite crystal preferred orientations (CPO). This study analyzes the CPOs of antigorite and olivine in variably serpentinized samples of antigorite serpentinite from three localities in Southwest Japan, using U-stage, EBSD, and synchrotron X-rays. In all samples (010) poles show a maximum parallel to the lineation, and (001) poles concentrate normal to the foliation with a partial girdle about the lineation. (100) poles are less distinct and scatter widely. The three measurement methods give similar results, though orientation distributions from X-ray analysis which averages over larger sample volumes are more regular and weaker than U-stage and EBSD which focuses on local well-crystallized grains. In olivine-bearing serpentinite, the olivine CPO does not appear to control the antigorite CPO, though there are some topotactic relationships. The antigorite CPO formed contemporaneously with serpentinization and shear deformation. Based on our analyses, in a subduction zone mantle wedge, the (010) pole of antigorite is parallel to the direction of the subduction, and (001) lattice planes are parallel to the interface of the subducting oceanic plate. By averaging single crystal elastic properties over orientation distributions wave velocities have been calculated. Fast P velocities are parallel to the subduction direction and slow velocities are perpendicular to the subducting plate with an anisotropy of 10–15%.

1. Introduction

Antigorite serpentinites with crystallographic preferred orientations (CPO) exhibit strong elastic anisotropy (e.g., Kern, 1993; Kern et al., 1997; Mookherjee and Capitani, 2011; Watanabe et al., 2007). The CPO is considered to cause shear-wave anisotropy, with trench-parallel fast directions observed in subduction zones (Jung, 2011; Katayama et al., 2009). The type of antigorite CPO and the degree of mantle wedge serpentinization are important factors in understanding the nature of subduction zones.

Two different antigorite CPO patterns have been described from foliated antigorite serpentinites in previous studies. Both patterns have (001) lattice planes of antigorite parallel to the foliation. But the L-a-type (defined by Nishii et al., 2011) has antigorite [100] axes parallel to the lineation (Bezacier et al., 2010; Padrón-Navarta et al., 2012; Van de Moortèle et al., 2010), whereas the L-b-type has [010] axes parallel to the lineation (Hirauchi et al., 2010; Jung, 2011; Nishii et al., 2011, Soda and Takagi, 2010; Watanabe et al., 2011). The L-a-type is also reported from the experimental deformation study of antigorite serpentinite by Katayama et al. (2009). The reasons for the two different CPO patterns, and mechanisms for the antigorite CPO formation remain unclear.

There are several models for antigorite CPO formation. Boudier et al. (2010) proposed a topotactic formation of antigorite CPO from olivine, based on transmission electron microscopy (TEM) studies of the relationship of the crystallographic orientations of host olivine and newly formed antigorite grains in samples from the Colorado Plateau xenoliths. They concluded that the source peridotite CPO defines the antigorite serpentinite CPO. Morales et al. (2013) demonstrate the transformation of fabric patterns from olivine to antigorite based on the topotactic relationships. Plümper et al. (2012) described an olivine-bearing antigorite serpentinite from the Leka Ophiolite Complex, Norway, and concluded that antigorite serpentinization is initiated along sub-grain boundaries in olivine, supporting the topotactic model.

Plastic crystal deformation has been suggested as a mechanism of CPO formation, based on the results of deformation experiments in which antigorite serpentinites develop CPOs from randomly oriented antigorite (Chernak and Hirth, 2010; Hilairet et al., 2007; Katayama et al., 2009). These results imply that in nature, static antigorite serpentinization precedes shear deformation. However, Nozaka (2005) and Mizukami and Wallis (2005) reported the direct formation of foliated antigorite serpentinite from the Happo-one ultramafic

* Corresponding author.
E-mail address: nahco3@staff.kanazawa-u.ac.jp (Y. Soda).

0040-1951/$ – see front matter © 2013 Elsevier B.V. All rights reserved.
http://dx.doi.org/10.1016/j.tecto.2013.12.016

complex and the Higashi-Akaishi peridotite body, Japan. There is uncertainty regarding the formation mechanism and the processes that result in the serpentinization of peridotite.

To develop a better understanding of antigorite CPOs, we measured antigorite crystal orientations in three types of foliated antigorite serpentinite using three different methods: optical microscopy with a U-stage, electron back scatter diffraction (EBSD) with a scanning electron microscope, and synchrotron X-ray diffraction. We also examined with EBSD and U-stage the relationship between olivine and antigorite crystal orientations to elucidate the formation mechanism of antigorite CPO during the initial stage of serpentinization. The EBSD measurements of antigorite CPO are difficult, since antigorite is a physically weak mineral with significant bending (Nishii et al., 2011). Synchrotron X-ray measurements have emerged as a powerful tool for measuring CPO of phyllosilicate minerals in shales (e.g., Wenk et al., 2008, 2010) and are used here for comparison. The process of serpentinization and the antigorite CPOs are important considerations when drawing conclusions about elastic anisotropy in subduction zones.

2. Samples

We investigated the CPO of foliated antigorite serpentinite collected from three localities in Southwest Japan (Fig. 1). Serpentinite A is an olivine-bearing serpentinite mylonite from the Toba area. This serpentinite was also used to study the relationship between crystal orientations in olivine and antigorite, and the nature of the initial stage of serpentinization. Serpentinite B is a completely serpentinized mylonite from the Saganoseki area. Serpentinite C is a serpentinite schist from the Nagasaki area, with weak foliation and lineation compared to samples A and B. Brief descriptions of the samples are given below. The reference frame for foliated serpentinite is defined with the X direction parallel to the lineation, the Z direction normal to the foliation, and the Y direction normal to the XZ plane.

The three serpentinite bodies are associated with high-pressure type metamorphic rocks, which implies that serpentinization occurred in the subduction zones. There is no evidence that these bodies are affected by high temperature type metamorphism, such as granite intrusions. Thus,

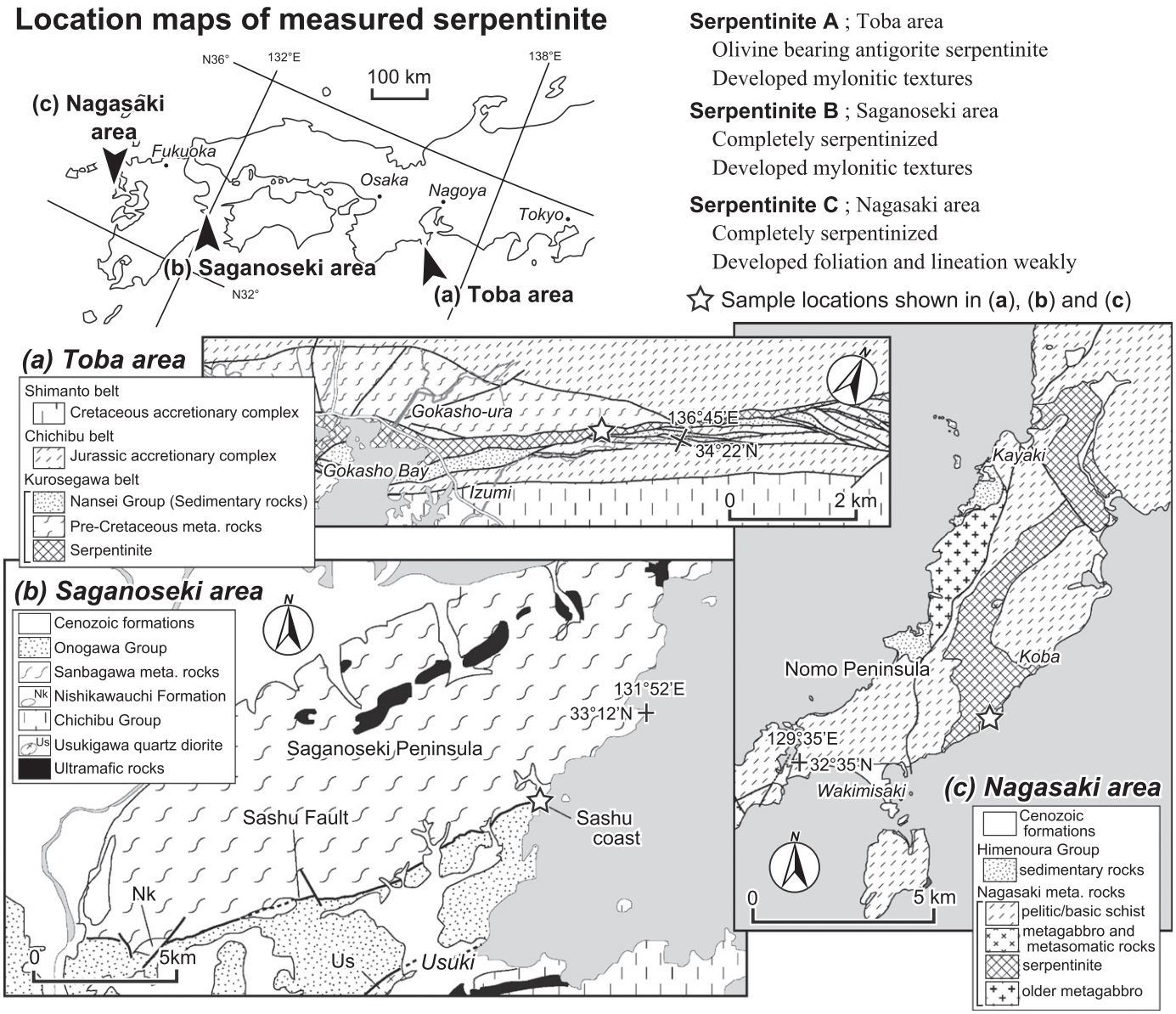

Fig. 1. Location maps and sample summary. (a) Geological map of Toba area modified after Saka et al. (1988). (b) Geological map of Saganoseki area after Teraoka et al. (1992). (c) Geological map of Nagasaki area after Nagasaki City (2013). Asterisks in each map indicating outcrops of measurement samples.

the serpentinites in this study are expected to record microstructures developed in the subduction zones.

2.1. Serpentinite A: olivine-bearing serpentinite mylonite from the Toba area

Lenticular serpentinite bodies intrude a Jurassic accretionary complex and pre-Cretaceous metamorphic rocks in the Toba area, southwest Japan (Fig. 1a) (Saka et al., 1988; Yokoyama, 1987). Occasionally, the serpentinite body contains blocks of schists that have undergone high-pressure metamorphism (Saka et al., 1988). Olivine-bearing serpentinite mylonites occur as massive blocks surrounded by incohesive serpentinite. The serpentinite mainly consists of antigorite and olivine, without bastite alteration of orthopyroxene. The serpentinite mylonite undergoes a later stage of transformation with local growth of chrysotile and lizardite and cataclastic deformation, which are dominant in the surrounding, incohesive serpentinite. Foliation of the sampled serpentinite mylonite strikes ENE–WSW and dips moderately to steeply to the northwest. Its

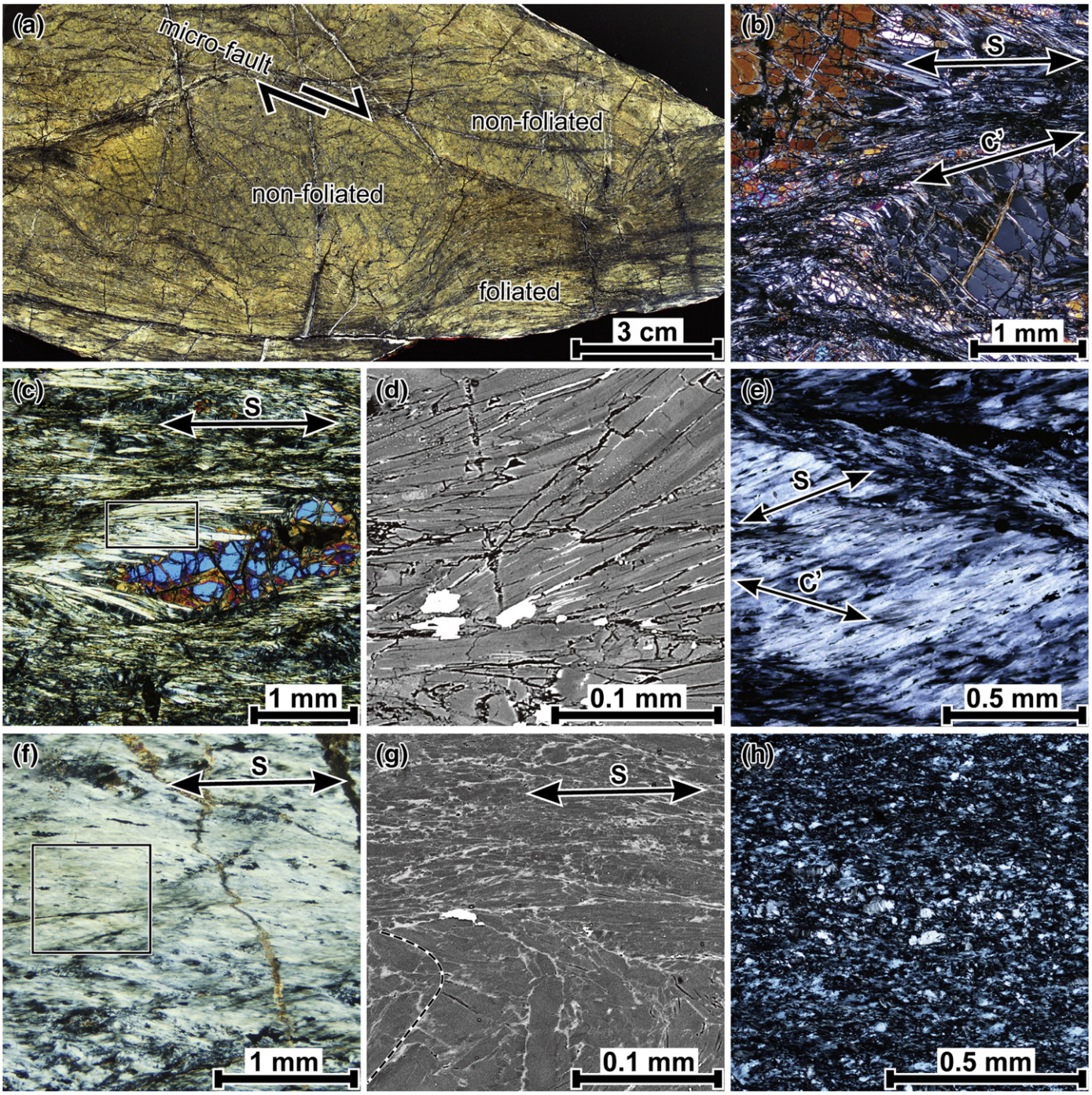

Fig. 2. Photograph of polished hand specimen (a), photomicrographs of thin sections (b), (c), (e), (f) and (h) and back scatter electron (BSE) images (d) and (g). (a)–(d) From serpentinite A (Toba area), (e)–(g) from serpentinite B (Saganoseki area) and (h) from serpentinite C (Nagasaki area). (a) Olivine-bearing serpentinite mylonite. The center of the specimen preserves peridotite texture (non-foliated), sheared by a micro-fault. (b) Porphyroclastic olivines and antigorite along S and C′ plane in serpentinite A. Cross polarized light (CPL). (c) Olivine grain in an antigorite matrix. Box indicates the region where EBSD measurements were performed. CPL. (d) Dragged and fractured antigorite in serpentinite A. BSE image. (e) Needle-shaped antigorite with S–C′ fabric in serpentinite B. CPL. (f) EBSD measurement area of serpentinite B (box indicated). CPL. (g) Micro-fold axis (indicated by broken line) of serpentinite B. Fe-rich antigorite (light gray) infilling fractures and along the grain boundaries of normal antigorite (gray). BSE image. (h) Antigorite in serpentinite C. CPL.

strike is sub-parallel to the distributional direction of the serpentinite body (Fig. 1a).

The degree of antigorite serpentinization and deformation changes drastically within the massive block at the outcrop scale. Where antigorite serpentinization is weak, the serpentinite preserves the original peridotite texture (non-foliated). Where antigorite is dominant, the serpentinite possesses both a penetrative foliation and lineation, and is mylonitic. Locally, the serpentinite mylonite wraps around non-foliated zones, as observed in hand samples (Fig. 2a). The boundary between the non-foliated zone and the mylonite is sharp, and the non-foliated zone is cut by a micro-fault (Fig. 2a).

The serpentinite mylonite consists of antigorite, olivine, and altered Cr-spinel, with secondary clinopyroxene and magnetite. Elongate olivine grains and needle-shaped antigorite define the foliation and lineation. Olivine and antigorite form mylonitic textures with porphyroclasts and a composite planar fabric.

Olivine grain size varies from 1.5 to 0.1 mm. Occasionally, olivine grains are "cleavable" (Hawkes, 1946; Nozaka and Ito, 2011), where olivine grains with parting (similar to cleavage) alternate with needle-shaped antigorite. A few olivine grains have developed sub-grain boundaries normal to the foliation. Antigorite grains define foliations (S and C′ planes) (Fig. 2b, c), and crystallized in olivine pull-aparts and along grain boundaries. In the XY sections, long axes of needle-shaped antigorite grains grow occasionally oblique to the lineation. Antigorite associated with "cleavable olivine" bends along the foliation or shear bands (C′ plane). In back scatter electron images (BSE image), bent antigorite grains contain open fractures oriented perpendicular to their long axes (Fig. 2d). Partly prismatic clinopyroxene grains are scattered in the antigorite matrix. The long axes of clinopyroxenes are randomly oriented, indicating post-tectonic crystallization. Relic olivine in antigorite serpentinite was altered to chrysotile and lizardite during low-temperature serpentinization.

Veins of fine-grained olivine (<0.01 mm) occur along the C′ planes. Occasionally, veins cut the mylonitic foliation, indicating that veining occurred by syn- or post-serpentinite mylonitization. Veins consist mainly of olivine with lesser diopside, magnetite, and antigorite. Yokoyama (1987) estimated the temperature of vein formation as 400 °C, based on the Mg–Fe equilibrium in olivine–clinopyroxene assemblages.

2.2. Serpentinite B: serpentinite mylonite from the Saganoseki area

The serpentinite from the Saganoseki area (Fig. 1b) intrudes along the Sashu Fault, which is the boundary between the high-pressure Sanbagawa metamorphic rocks and the Cretaceous forearc basin cover of the Onogawa Group. This serpentinite has been described in detail by Soda and Takagi (2010). The measured sample is collected from a serpentinite block resisting erosion at the Sashu coast. The foliation of the serpentinite strikes ENE–WSW, and dipping moderately to steeply to the south. Its direction is sub-parallel to the strike and dip of the Sashu Fault and the schistosity of metamorphic rocks.

The serpentinite mylonite mainly consists of antigorite with minor Cr-spinel and magnetite, and an alteration assemblage of carbonate minerals, talc, and sulfides. Oriented antigorite and magnetite grains define the foliation and lineation. Needle-shaped antigorite defines an S–C′ fabric (Fig. 2e), occasionally micro-folds are observed (Fig. 2g). Antigorite microstructures are often heterogeneous, in some parts parallel to the S plane and in other regions randomly orientated (Fig. 2f). The iron content in antigorite ranges widely, being low in needle-shaped antigorite and high in antigorite that crystallized in veins, along antigorite grain boundaries, and within fractures of iron-poor needle-shaped antigorite, as observed in BSE images (Fig. 2g) (Soda and Takagi, 2010).

Based on thin section examination of relatively coarse-grained antigorite (from the XZ, YZ and XY sections), the average aspect ratios for antigorite needles are 1:0.2:0.1 ([010]:[100]:[001]). This is significant for the elastic property averaging. However, accurate grain size distributions of antigorite cannot be measured, since most antigorite grains show undulose extinction and their grain boundaries are unclear. The BSE image (Fig. 2g, top) indicates the grain size of Fe-antigorite, infilling the boundaries, is <5 μm.

2.3. Serpentinite C: serpentinite schist from the Nagasaki area

The serpentinite schist from the Nagasaki area (Fig. 1c) occurs within the Nagasaki (Nishisogino) metamorphic rocks, which have undergone high-pressure metamorphism (Nishimura, 1998). Metasomatic rocks occur in the boundary zone between serpentinite and metamorphic rocks (Nishiyama, 1990; Shigeno et al., 2012). In the outcrop, the serpentinite is characterized by bastite-rich layers that define the foliation and lineation, and these develop heterogeneously. The foliations of serpentinite around the outcrop strike NE–SW and dipping slightly to the northwest. The surrounding metamorphic rocks also develop sub-horizontal schistosities (Nagasaki City, 2013).

The serpentinite consists of antigorite, metamorphic diopside, magnetite and chlorite. Antigorite is fine-grained, fibrous to needle-shaped, with obscure grain boundaries (Fig. 2h). It is difficult to measure antigorite CPO in serpentinite C by U-stage. However, optical microscope observations, with the gypsum plate inserted, show that the antigorite grains have similar crystallographic orientations. In BSE images, antigorite appears relatively homogenous in terms of chemical composition, and is free of cracks and fractures. Antigorites of elongated shape transformed from pyroxene (bastite) are not fine-grained, suggesting that pyroxene altered after the shear deformation.

3. Methods to measure crystallographic preferred orientation

3.1. Universal stage

An optical microscope equipped with a U-stage is a classical tool used to measure crystal orientations (Passchier and Trouw, 1996; Wenk, 1985). We used a microscope Nikon Optiphot, objective lens of 10 or 20 times power, combined with a U-stage of four rotation axes to determine the preferred orientation of olivine in serpentinite A and, of antigorite in serpentinites A and B. We measured the orientations of indicatrix axes of the minerals. The pole figures are plotted by the software BEARTEX (Wenk et al., 1998) and commercial software SpheriStat. The contours in the pole figure are shown as multiples of a random distribution (m.r.d.) obtained by Gaussian averaging (7.5° filter). The U-stage data are converted to Euler angles by the program developed by Wallis et al. (2011). In antigorite, only the crystallographic axis b = [010] is strictly congruous with the optic axis [nγ]; however, crystallographic axes c = [001] and a = [100] are approximately parallel to the optic axes of [nα] and [nβ] (Deer et al., 1992). For U-stage measurements we use zone axes [uvw] rather than poles to lattice planes (hkl) for representation. However, since the lattice angle β for monoclinic antigorite is close to 90° (91.6°), the two representations are roughly equivalent.

3.2. EBSD

EBSD measurements of olivine and antigorite on serpentinites A and B were performed with a ZEISS EVO MA10 variable vacuum SEM and a TSL OIM data collection system, at the Department of Earth and Planetary Science, University of California, Berkeley. Thin sections were polished with 0.25 micron diamond paste and subsequently polished with colloidal silica for up to 2 min. For indexing we used the antigorite structure of Uehara (1998) and the olivine structure of Artioli et al. (1995), with 20 high intensity reflections. The microscope was operated at 25 kV and a probe current 2 ~ 3 nA with a working distance of 20–25 mm, and 10 Pa vacuum. Crystal orientations were measured as continuous scans with 2–10 micron steps (automatic indexing). Manual indexing, of individual patterns to verify correct

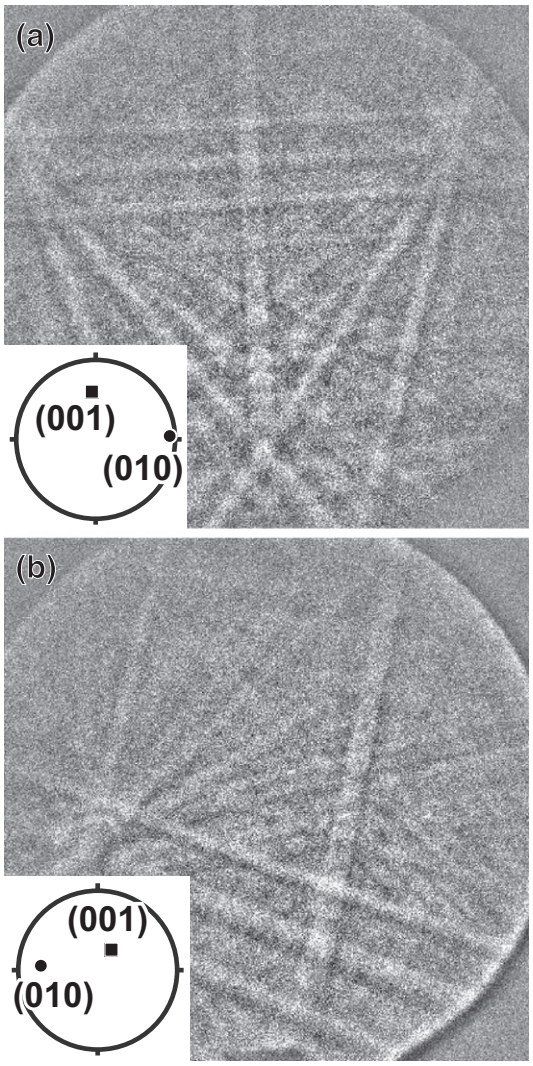

Fig. 3. Selected antigorite Kikuchi patterns of antigorite. Stereographic projections indicate crystal orientation.

crystallographic indexing, was also performed in one sample, to check the quality of automatic indexing. In the pole figures, only orientation data satisfying a threshold confidence index value (CI) >0.01, and image quality value (IQ) >500 were used. Thus the number of data points does not reflect the number of grains. Two antigorite Kikuchi patterns with corresponding crystal orientations are shown in Fig. 3, with sets of Kikuchi bands parallel to (001). Orientation distributions were calculated from individual orientations. This, as well as pole figure calculations and plotting was done with the software BEARTEX (Wenk et al., 1998).

3.3. Synchrotron X-rays

Synchrotron X-ray diffraction measurements were performed on serpentinites B and C at the high-energy beamline ID-11-C of APS, at Argonne National Laboratory. The method is described in detail in Wenk et al. (2008) and Wenk et al. (2010). The monochromatic wavelength was 0.10803 Å. The beam size used was 0.5 × 0.5 mm. Diffraction images were collected with a Perkin Elmer amorphous silicon large area detector with 2048 × 2048 pixels.

The sample slabs, 1 mm thick, were cut to reveal XZ sections, and were mounted with a metal rod on a goniometer. A relatively homogeneous area was selected for the analysis and the sampled volume is ~0.25 mm^3. The slab foliation was parallel to the horizontal axis of the goniometer and seven images were recorded at different tilt angles, from −45° to +45° in 15° increments. This provides a satisfactory pole figure coverage. Typical diffraction images for the two samples are shown in Fig. 4. Intensity variations along the Debye rings immediately indicate preferred orientation, stronger for serpentinite B (Fig. 4a) than for serpentinite C (Fig. 4b).

The diffraction images were then processed with the Rietveld method implemented in the software package MAUD (Lutterotti et al., 1997; Lutterotti et al., 2013), refining parameters such as background, lattice, grain size and preferred orientation. The refinement was based on the antigorite structure of Uehara (1998). For the Rietveld refinement the first setting with [001] as symmetry axis has to be used for monoclinic symmetry (Matthies and Wenk, 2009) but for representation we use the more conventional second setting (with [010] as symmetry axis). Fig. 5 shows the stacks of diffraction patterns, obtained by a 10° angular integration, for the 0° tilt diffraction images. At the bottom are the experimental data and above is the Rietveld fit. We see the strong intensity variations already evident in the diffraction images (Fig. 4) but also observe the excellent intensity fit for most reflections, indicating a reliable CPO extraction. Some diffraction peaks of antigorite are labeled. A few peaks with no preferred orientation are due to

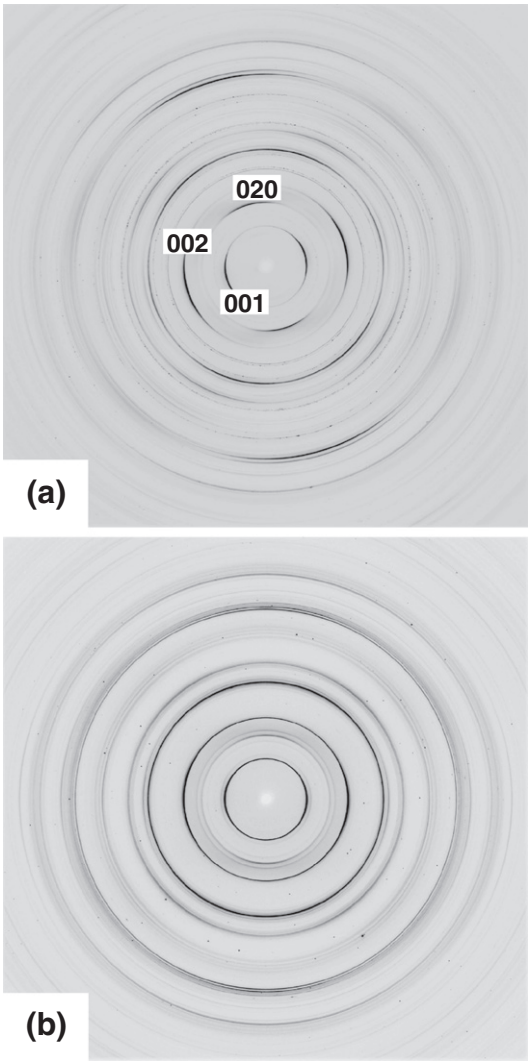

Fig. 4. Typical X-ray synchrotron diffraction images. (a) Serpentinite B, showing strong preferred orientation of antigorite. (b) Serpentinite C with weaker preferred orientation. Some Debye rings are indexed.

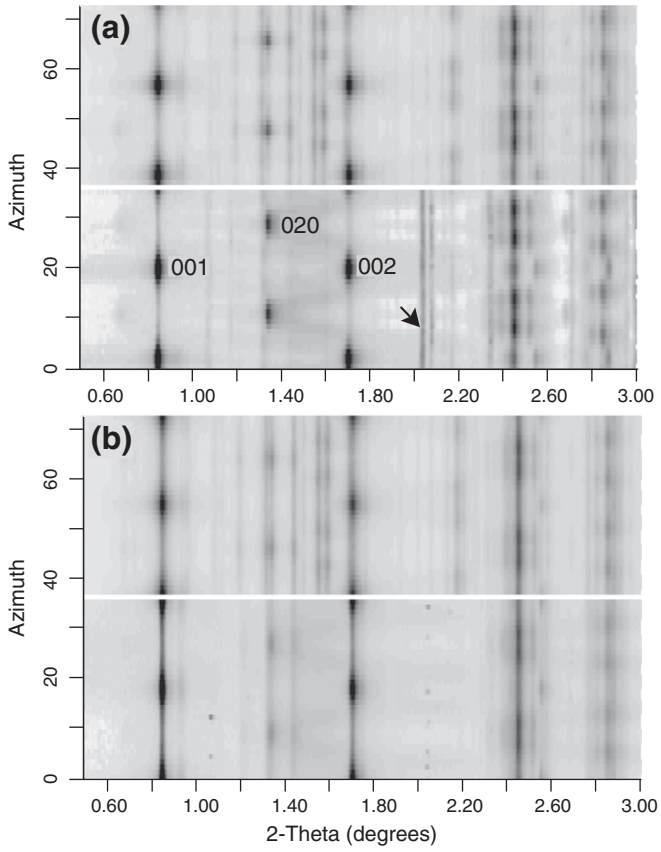

Fig. 5. Stack of synchrotron diffraction patterns (bottom) and corresponding Rietveld fit (top) for serpentinite B (a) and C (b). Note the strong intensity variation of diffraction peaks with azimuthal angle (vertical axis). Some diffraction peaks of antigorite are labeled. Arrow points to lines from carbonate accessories.

accessories (especially magnesite in serpentinite B, marked with arrow). Some calculated antigorite peaks are more intense than the experimental data, especially in the 2θ range 1.3°–1.6°. This is attributed to significant stacking disorder of the antigorite in serpentinites, compared with the single crystal of Uehara (1998). Refined lattice parameters for antigorite in serpentinite B are a = 43.636 (2) Å, b = 9.2062 (4) Å, c = 7.2688 (2) Å, β = 91.629 (4)° and in serpentinite C a = 43.590 (2) Å, b = 9.2156 (5) Å, c = 7.2746 (2) Å, β = 91.573 (4)° with standard deviations in parentheses. The grain sizes are 40–50 nm for both samples. This corresponds to the average coherently scattering domain size which is difficult to compare with optical data for these highly bent and fragmented crystallites with significant stacking disorder. It is obtained to achieve an optimal fit of the diffraction peak shape.

4. Crystal preferred orientations of antigorite and olivine

4.1. Olivine CPOs from serpentinite A

Olivine pole figures for serpentinite A, measured by U-stage, are shown in Fig. 6a, b. Measured olivine grains are porphyroclastic grains from less-serpentinized parts of the samples. Olivine CPO (1) (Fig. 6a) was measured from 100 grains in two thin sections (the same hand specimen used for EBSD measurements), while olivine CPO (2) (Fig. 6b) was measured from 191 grains in four thin sections.

The two samples show similar fabric patterns with a pronounced asymmetry relative to the macroscopic coordinates. The [100] axes are concentrated in a maximum close to the Y direction, the [010] axes form a girdle about the [100] maximum with a subsidiary concentration between X and Z. The [001] orientations of the olivine CPO (2) form a weak point maximum at 10°–20° clockwise from the X direction in the XZ plane, and a diffuse girdle about the Z direction. The [001] orientation of olivine CPO (1) forms a weak point maximum rotated 10°–20° counterclockwise from the Z direction in the XZ plane.

4.2. Antigorite CPOs and relationships with host olivine in serpentinite A

Fig. 6c displays U-stage measurements for 105 grains of antigorite near an olivine porphyroclast in two thin sections. The pole figures show that the [100] axes of antigorite are concentrated in the Y direction, the [010] axes are parallel to the lineation, and [001] is normal to the foliation, with a slight asymmetry but overall more symmetrical than olivine. Pole maxima for [010] are very strong (15 m.r.d.).

Fig. 6d, e is the pole figures of antigorite for serpentinite A based on EBSD measurements with automatic indexing (Fig. 6d) and manual indexing (Fig. 6e). The measured area 0.9 × 0.4 mm was scanned with 2 micron steps in the automatic indexing and is shown in Fig. 2c. It is a relatively homogeneous antigorite matrix near an olivine porphyroclast. 108,113 points are measured and 70,143 points (65%) satisfy the threshold values for the pole figures. Basically, the CPO patterns are similar to those of the U-stage measurements. The (100) pole figure displays a weak concentration in the Y direction, the (010) pole figure shows a point maximum parallel to the lineation X and the (001) pole figure has a point maximum normal to the foliation Z and a weak partial girdle about the lineation (Fig. 6d). Manual indexing of 206 grains was also performed for the same area of the automatic scan. The plots (Fig. 6e) indicate that manual indexing yields a similar CPO pattern as the automatic indexing (Fig. 6d) but, since for manual indexing a few large grains were selected, the distribution is more regular and maximum pole densities are higher (Table 1).

We measured the CPOs of antigorite and adjacent porphyroclatic olivine by U-stage and EBSD, to discuss the relationship between their crystal orientations at the initial stage of serpentinization. In the measured areas, needle-shaped antigorite grows in the rims and the edges of porphyroclastic olivine. Fig. 7 shows the results of measurements by U-stage. Fig. 7a, b is divided data that were combined in Fig. 6c. Notice that olivine plots in Fig. 7 are from domains within the host olivine, separated by fractures or serpentine veins. The [010] axis of antigorite is parallel to the lineation in all three measurements (Fig. 7a, b, and c). Also shown are the orientations of olivine in the domains. As is obvious all three olivine grains have very different orientations.

EBSD measurements performed on an aggregate of olivine and antigorite are illustrated in Fig. 8. 4488 points are measured from 0.67 × 0.65 mm with 10 micron steps (Fig. 8a). 3512 points are identified as olivine (Fig. 8b), 975 points as antigorite (Fig. 8c). Pole figures of olivine (Fig. 8d) are based on 2075 points satisfying the threshold values, and pole figures of antigorite (Fig. 8e) are based on 436 points. The large olivine cluster consists of several subgrains, as is obvious by interference colors (Fig. 8a) and an EBSD orientation map (Fig. 8b). The host olivine grain is rotated asymmetrically (Fig. 8d). Pole figures of antigorite are shown in Fig. 8e. Antigorite poles of (010) show two maxima: sub-parallel to the lineation (s2 in Fig. 8e) and at a relatively high angle to the XZ section (s1 in Fig. 8e). The s1 and s2 locations in the thin section are indicated in Fig. 8c. Antigorite s1 is surrounded by olivine o1 (Fig. 8b). There is an apparent orientation relationship o1–s1 with [100] olivine parallel to [100] antigorite, [010] olivine parallel to [001] antigorite and [001] olivine parallel to [010] antigorite (Fig. 8d, e). No clear relationships are observed between olivine o3 and antigorite s2, where antigorite needles are aligned more parallel to the lineation. The antigorite CPO of s2 is similar to the pattern from the olivine free part (Fig. 6d). A summary of the relationships of crystal orientation between antigorite and host olivine is given in Fig. 9.

4.3. Antigorite CPOs from olivine free serpentinite (serpentinites B and C)

We carried out U-stage measurements of 100 grains in relatively coarse-grained antigorite aggregates in foliation-parallel (XY) thin

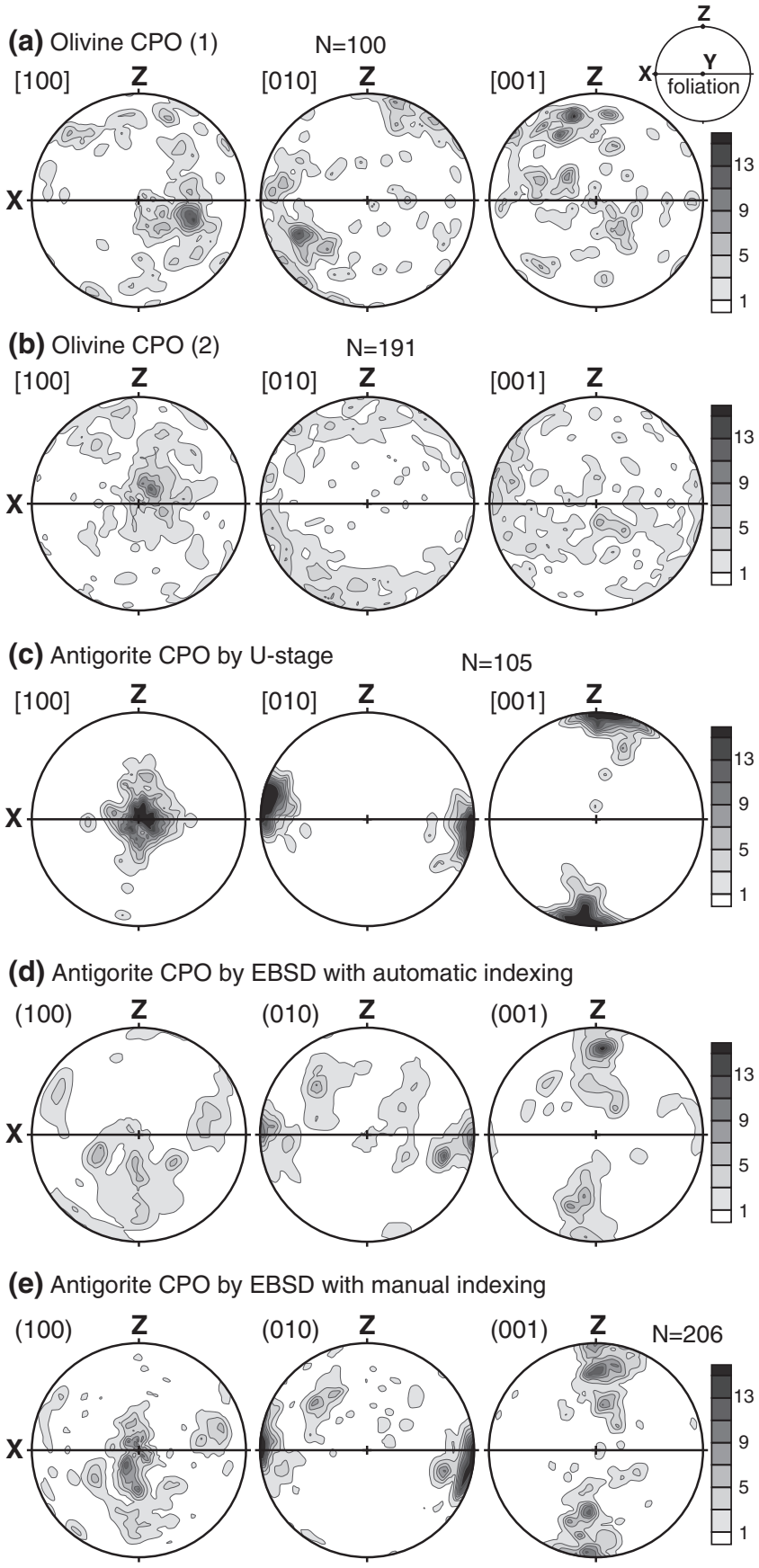

Fig. 6. Pole figures of olivine CPOs (a, b) and antigorite CPOs (c, d, e) from serpentinite A. Upper hemisphere equal-area projections. The X direction presents the lineation, the Z direction represents normal to the foliation (shown in upper right). Pole densities are expressed in multiples of a random distribution (m.r.d.). (a, b) Olivine CPOs measured by U-stage measurement. (c) Antigorite CPOs by U-stage measurement. (d) Antigorite CPOs by EBSD with automatic indexing. (e) Antigorite CPOs by EBSD with manual indexing from the same area as in (d).

Table 1
Pole figure maxima and minima for antigorite in multiples of random distribution (m.r.d.).

	Antigorite (100)		Antigorite (010)		Antigorite (001)	
	Max.	Min.	Max.	Min.	Max.	Min.
Serpentinite A						
U-stage	22.8	0.0	35.5	0.0	31.6	0.0
EBSD	7.2	0.0	12.5	0.0	19.1	0.0
EBSD (manual)	13.1	0.0	26.3	0.0	12.3	0.0
Serpentinite B						
U-stage	13.4	0.0	34.1	0.0	20.2	0.0
EBSD	5.1	0.0	8.8	0.0	9.6	0.1
X-ray	2.4	0.6	5.9	0.2	6.0	0.2
Serpentinite C						
X-ray	1.6	0.7	2.6	0.4	4.2	0.3

sections of serpentinite B (Fig. 10a). The [010] orientation obtained is a maximum parallel to the lineation X, while [001] poles are concentrated normal to the foliation, forming a weak partial girdle about the lineation. [100] forms a point maximum parallel to Y with a weak girdle about the lineation X. This fabric pattern is similar to that obtained in serpentinite A (Fig. 6c, d). Soda and Takagi (2010) also reported the same CPO pattern from antigorite serpentinite in the same outcrop (The labels in Fig. 6 of their paper are misprinted. The correct labels of the optic elasticity axes are alpha, beta and gamma from left to right).

Fig. 10b shows the pole figures of antigorite obtained with EBSD measurements. Scans were taken from an area 0.83 × 0.83 mm (2 micron steps) of fine-grained and well-oriented antigorite (Fig. 2f). 173,055 points are measured, and 51,207 points (30%) are used in the pole figure reconstruction (Fig. 10b). CPO patterns by EBSD measurement are similar

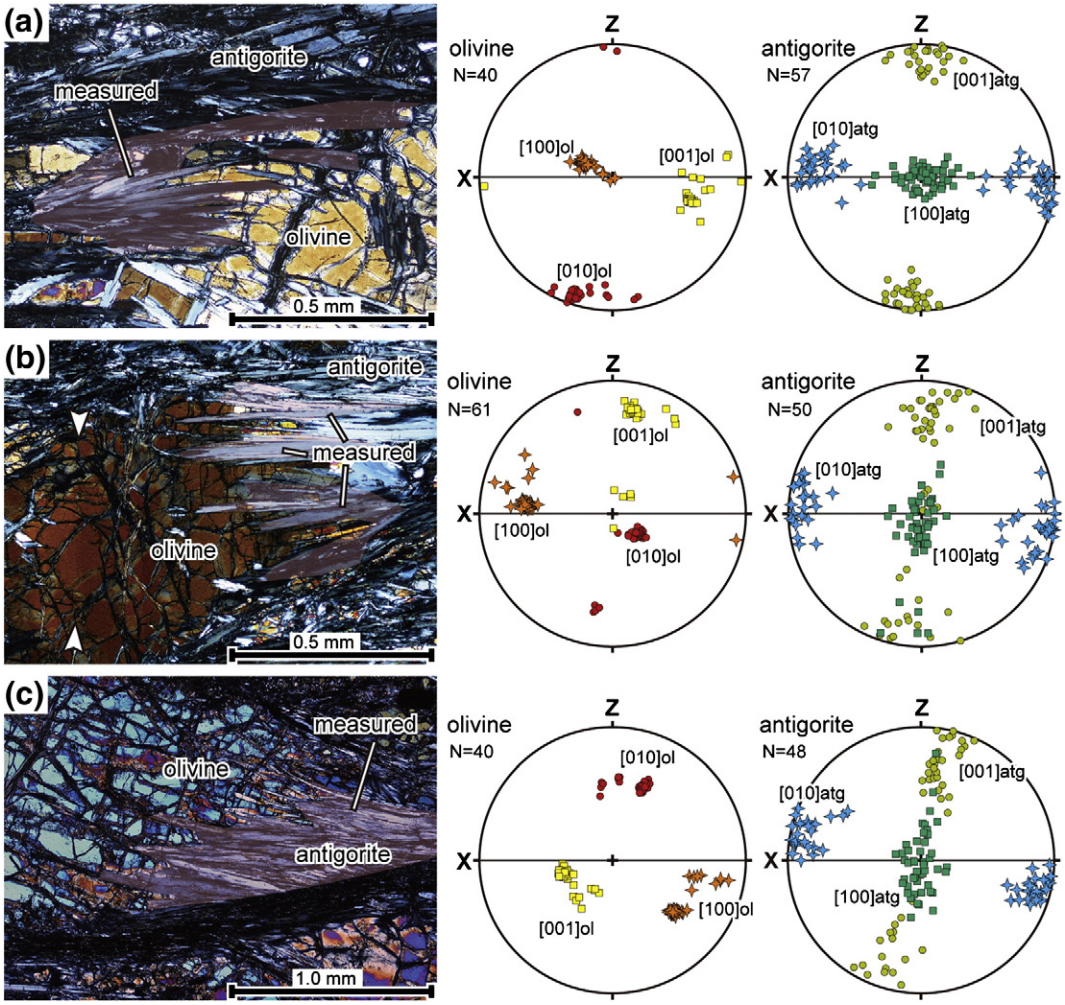

Fig. 7. Crystal orientation relationships between olivine and antigorite in serpentinite A, as measured by U-stage. Upper hemisphere equal-area projections. Left column are photomicrographs showing measured area, center column are pole figures of olivine orientation and right column pole figures of antigorite. White arrows in (b) indicated sub-grain boundary of olivine.

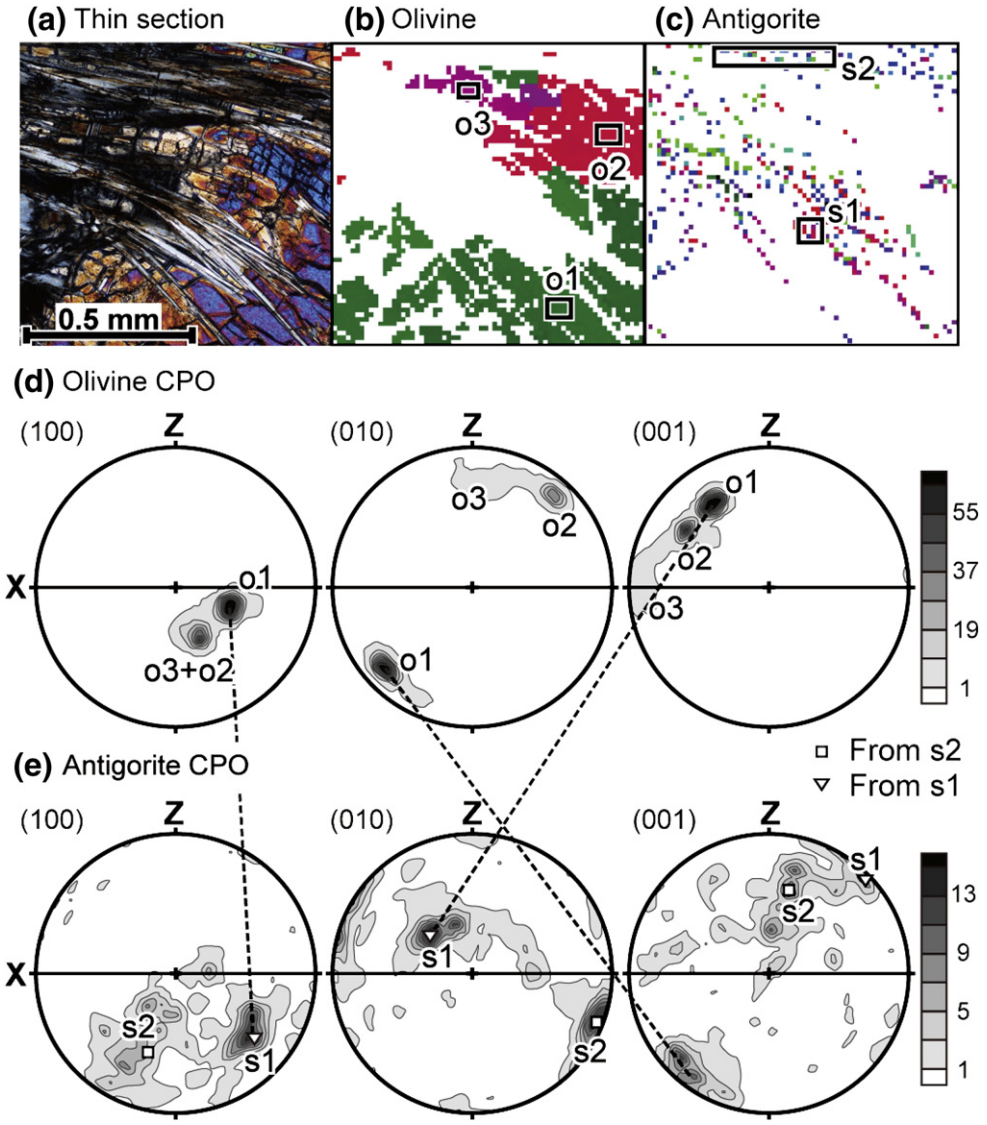

Fig. 8. Detailed observation of crystal orientation relationships between olivine and antigorite in serpentinite A, as measured by EBSD. (a) Photomicrograph of measured area. (b) Olivine orientation map (Euler angle gamma); o1, o2 and o3 indicate the areas yielding counter peaks in pole figures of olivine (d). (c) Antigorite orientation map (Euler angle gamma); s1 and s2 indicate the area yielding counter peaks in pole figures of antigorite (e). (d, e) Pole figures of host olivine (d) and needle shape antigorite (e). Upper hemisphere equal-area projections. Pole densities are in m.r.d.

to the CPO from U-stage, but pole densities are reduced (Fig. 10b. Table 1). A weak point maximum of (100) poles appears sub-parallel to the lineation X. A maximum of (001) poles is slightly tilted relative to Z.

The results of the synchrotron X-ray data analysis are shown in Fig. 10c for serpentinite B and Fig. 10d for serpentinite C. For both samples (001) the pole figures show a well-defined maximum normal to the foliation Z, and weak partial girdle about the lineation X. The (010) pole figures display a concentration in the lineation and weak girdle about the Z direction. The (100) pole figures are less defined. There is a weak peak maximum normal to the XZ plane, with a girdle around Z. Serpentinite B has a stronger CPO than serpentinite C.

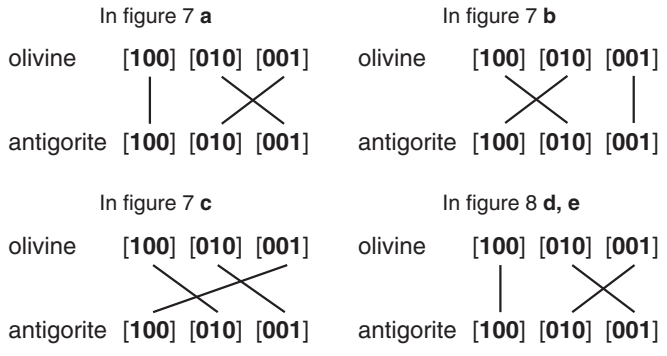

Fig. 9. Orientation relationships between olivine and antigorite in serpentinite A.

It is interesting to compare the results from different measurement techniques for sample B. The overall CPO pattern is similar, but much smoother for synchrotron X-rays than for U-stage. EBSD data are intermediate. Also, the orientation densities are much higher for the U-stage and EBSD as shown in Table 1. This is not surprising since the U-stage and EBSD focus on individual antigorite clusters with high local orientations as expressed in microstructures (e.g. Figs. 2e, g and 8a), while synchrotron X-rays average over larger volumes and include also small grains. Obviously, the U-stage measurements are only possible on coarse grains, representing 100 points from ~1 × 1 mm. The EBSD measurements neglect 70% of the poorly indexed point from 0.83 × 0.83 mm. X-rays are more representative for the bulk serpentinite orientation patterns. Significant is a large portion of randomly oriented grains (pole density minima in Table 1 range from 0.2 to 0.7 m.r.d.).

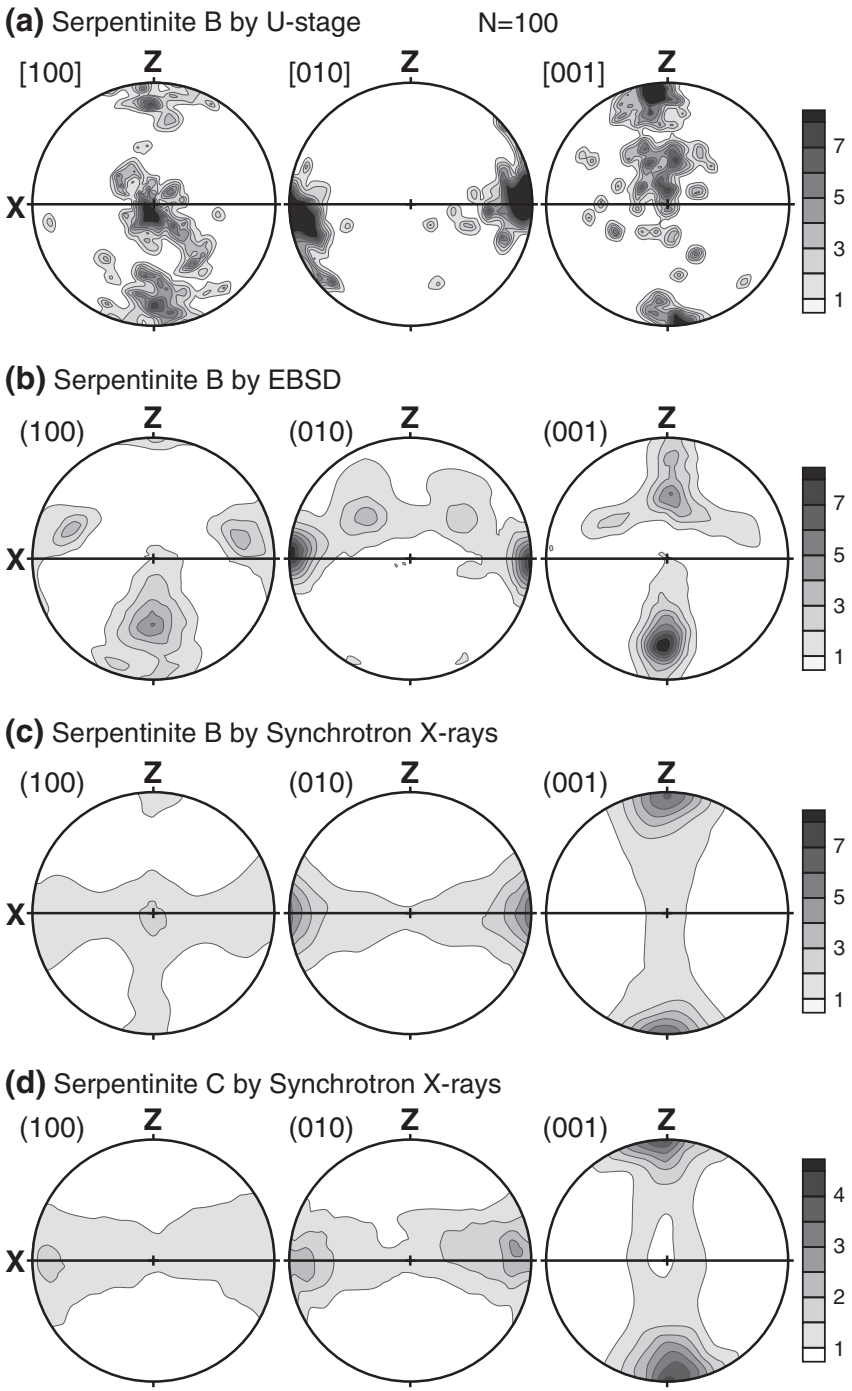

Fig. 10. Pole figures of antigorite. Upper hemisphere equal-area projections, pole densities in m.r.d.. (a) Serpentinite B with U-stage measurement. (b) Serpentinite B with EBSD measurement. (c) Serpentinite B measured by synchrotron X-rays. (d) Serpentinite C measured by synchrotron X-rays.

5. Discussion

5.1. Antigorite CPO in initial stage of serpentinization

Here we focus on the relationships of crystal orientation between olivine and antigorite to discuss the initial stage of serpentinization. The observed olivine CPO in serpentinite A (Fig. 6a, b) corresponds to the results from experimental studies of the B-type fabric (Jung and Karato, 2001; Jung et al., 2006), characterized by a [100] point maximum parallel to Y, although there is asymmetry which can be attributed to local heterogeneities (Fig. 2a, b). This fabric forms under relatively water-rich conditions as may be the case in subduction zones (Jung et al., 2006). It is important to note that the peridotite possessed an olivine CPO before serpentinization (Fig. 6a, b). Olivine CPOs of B-type in foliated serpentinized peridotites have been reported from the Higashi-Akaishi peridotite body of SW Japan by Wallis et al. (2011).

Boudier et al. (2010) describe the topotactic relationships between antigorite and olivine, based on TEM analyses. In this case, source peridotite shows A-type fabric (Morales et al., 2013). The main topotaxy is [100]ol//[001]atg, [010]ol//[100]atg and [001]ol//[010]atg, and the secondary topotaxy is [100]ol//[100]atg, [010]ol//*c*[001]atg and [001]ol//[010]atg. The second one is similar to one of the relationships described here (Figs. 7a, 8 and 9). They suggested that the CPO fabric of host peridotite defines the CPO of antigorite serpentinite. At the scale of the

thin section of our study, the topotactic relationships reported by Boudier et al. (2010) cannot explain the relationship between the bulk CPOs of olivine (Fig. 6a, b) and antigorite CPO (Fig. 6c, d, and e) in serpentinite A from Toba. If we adapt their main topotaxy to our olivine CPO (B-type fabric), we would expect antigorite [001] axes perpendicular to the XZ section, which is inconsistent with antigorite [001] normal to the foliation observed here (Fig. 6c, d, and e).

Around porphyroclastic olivine, the secondary topotactic relationship of Boudier et al. (2010) is observed in our study (Figs. 7a and 8d, e). The optic and EBSD observations indicate that needle-shaped antigorite grains are cracked and have been dragged along shear bands (Fig. 2b, d). Detailed observations in olivine–antigorite aggregates (Fig. 8) indicate that the antigorite orientation is changed during deformation so that [010] becomes parallel to the lineation and [001] normal to the foliation. The topotactic relationships between olivine and antigorite become erased during shear deformation as soon as antigorite grows. Bulk antigorite CPOs are no longer controlled by the olivine fabric pattern, which underwent shear deformation accompanied by serpentinization. Antigorite needles are rotated so that [010] becomes parallel to the shear direction.

Crystal plastic deformation has been proposed as a deformation mechanism of antigorite (Chernak and Hirth, 2010; Hilairet et al., 2007; Katayama et al., 2009; Padrón-Navarta et al., 2012; Vogler, 1987). However, the complicated crystal structure of antigorite and highly anisotropic grain shape limits crystal plastic deformation (Auzende et al., 2006). An alternative deformation mechanism, dissolution–precipitation, has also been proposed (Auzende et al., 2006; Wassmann et al., 2011). Fractures filled with Fe-rich antigorite in serpentinite B are an expression of dissolution–precipitation (Fig. 2g), at least in the last stage of the ductile deformation. Microstructures in all three samples investigated here suggest that antigorite has pervasively recrystallized. The growth and orientation of recrystallized antigorite may be controlled by nucleation and growth in a stress field (Kamb, 1961; Shimizu, 1992). Foliated serpentinite is directly formed from peridotite similar to the preferred orientation of mica in many metamorphic rocks. It suggests that crystal plastic deformation by dislocation glide may not be the dominant mechanism for antigorite CPO in the initial stage of antigorite serpentinization. However, further studies are needed to solve the deformation mechanism of antigorite serpentinite.

It is proposed that in subduction zones wedge mantles are serpentinized along the subducting oceanic plates, based on a seismic study of Cascadia (Bostock et al., 2002) and a calculation of thermal structure, such as SW and NE Japan, Aleutians and Cascadia (e.g., Hyndman and Peacock, 2003; Peacock and Hyndman, 1999). Accepting the model of wedge -mantle serpentinization along the subducting oceanic plate and assuming that simple shear was a dominant strain environment, based on our CPO measurements in the three Japanese serpentinites, it is proposed that antigorite (001) planes are parallel to the interface of the subducting plate, and the [010] directions are parallel to the subduction direction. This is consistent with the results of previous studies of Jung (2011) and Watanabe et al. (2011).

5.2. Comparing antigorite CPO patterns from three different localities

Looking at the thin sections, it is obvious that considerable heterogeneity exists in all three samples, with local shear bands and a wide range of antigorite grain sizes and grain orientations (Fig. 2). U-stage measurements selected coarse and well-crystallized grains. In the case of EBSD and also synchrotron X-rays we focused on relatively homogeneous local areas. As mentioned earlier the X-ray analysis averages over the whole volume, including microcrystalline antigorite with a much broader orientation distribution as illustrated in the stack of X-ray spectra (Fig. 5) with intensity, e.g. for (001), at all azimuthal angles, even perpendicular to the foliation plane. Nevertheless, it is very encouraging that all three entirely different techniques qualitatively produced similar results.

Particularly for serpentinite B (Fig. 10a, b, and c) the same pattern, L-b-type, was obtained with the three methods: U-stage, EBSD, and synchrotron X-ray. The (010) pole figures display a point maxima parallel to the lineation, and the (001) poles are concentrated normal to the foliation with a partial girdle about the lineation. The (100) pole figures are more disperse. In the EBSD measurements of serpentinite B, only 30% of the measured points satisfy the threshold values. The weaker fabric pattern from the X-ray measurements is attributed to the selective choice of grains in EBSD and U-stage measurements. Serpentinite C could only be measured with X-rays, due to the small grain size. The fabric pattern is very similar to that for serpentinite B, though weaker and a considerable amount of randomly oriented crystallites. The (001) maximum is 4.2 m.r.d.. The (100) pole figure and (010) pole figure with weak girdle distributions on the foliation (Fig. 10d) might indicate compressive stress normal to the foliation, since antigorite in serpentinite C does not show (or preserve) shear deformation features.

In comparing our results with previous studies of antigorite CPOs, we found that similar fabric patterns (L-b-type), have been observed for serpentinite from Ohmachi Seamount along the Izu–Bonin frontal arc (Hirauchi et al., 2010), serpentinite schists from Val Malenco, Italy and ultramafic rocks from Bettolina, Italy (Jung, 2011), the Higashi-Akaishi peridotite body of SW Japan (Nishii et al., 2011) and the Happone ultramafic complex of Central Japan (Watanabe et al., 2011), investigated by EBSD measurements, and the Saganoseki Peninsula in SW Japan (Soda and Takagi, 2010) by U-stage measurements. X-ray pole figure goniometer measurements from the Piemonte ophiolite of the Western Alps (Vogler, 1987), also have a similar pattern, with the (001) poles in a point maximum normal to the foliation, and the (010) poles weakly concentrated along the lineation and forming a girdle distribution.

However, our results differ from the experimental study of Katayama et al. (2009) and natural samples from Escambray Massif of Central Cuba (Bezacier et al., 2010; Van de Moortèle et al., 2010), and the Cerro del Almirez massif, Southern Spain (Padrón-Navarta et al., 2012) (L-a-type). In these EBSD studies, antigorite (100) pole figures show a peak parallel to the lineation, and (010) poles form a concentration normal to the XZ plane in the foliation.

Table 2
Elastic stiffness tensors for antigorite single crystal (GPa) (from Bezacier et al., 2010) and for serpentinites B and C using a self-consistent averaging.

Single crystal (from Bezacier et al., 2010)						
Antigorite second setting d = 2.62, aspect ratio 2–10–1						
i=	1	2	3	4	5	6
j = 1	208.4	66.2	15.9	0	2.4	0
2	–	201.6	5.0	0	−4.4	0
3	–	–	96.7	0	2.5	0
4	–	–	–	17.4	0	−13.1
5	–	–	–	–	18.3	0
6	–	–	–	–	–	65.0
Serpentinite B						
Self-consistent						
i=	1	2	3	4	5	6
j = 1	141.97	36.74	42.40	−0.46	0.63	0.51
2	–	105.41	38.22	−0.41	−0.15	0.04
3	–	–	123.31	−1.84	0.59	0.17
4	–	–	–	33.06	0.19	−0.02
5	–	–	–	–	43.29	−1.01
6	–	–	–	–	-	33.41
Serpentinite C						
self-consistent						
i=	1	2	3	4	5	6
j = 1	133.68	38.47	41.78	0.38	0.19	1.13
2	–	108.24	39.22	0.13	0.19	0.02
3	–	–	120.64	1.54	0.57	0.26
4	–	–	–	35.07	0.43	0.27
5	–	–	–	–	41.06	0.73
6	–	–	–	–	–	35.52

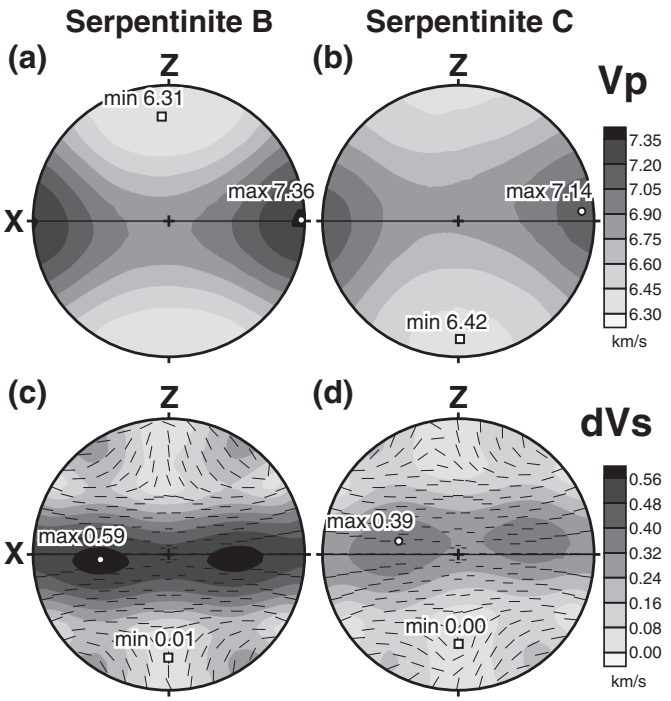

Fig. 11. Elastic wave propagation calculated from orientation distributions for serpentinite B (a, c) and C (b, d). Equal-area projection. (a, b) P-wave velocities (Vp in km/s), (c, d) shear-wave splitting (dVs in km/s). The polarization direction of the fast S-wave is indicated in (c, d).

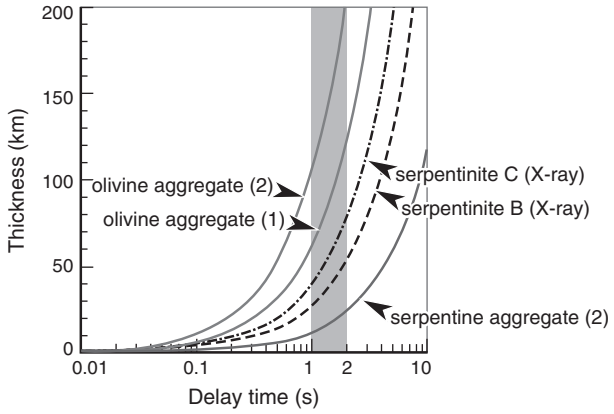

Fig. 12. Relationships between thickness of anisotropic layer (km) and shear-wave delay time (s) (after Katayama et al., 2009). Experimental results after (1) Zhang and Karato (1995) and (2) Katayama et al. (2009).

In the EBSD and X-ray measurements of serpentinite B, poles of (100) and (010) show weak girdle distribution about the lineation. Especially, in the EBSD measurements, the (100) poles also show a weak point maximum sub-parallel to the lineation. We have no data to decide if these grains, became oriented by crystal plasticity with [100](001) slip as proposed by Padrón-Navarta et al. (2012), or crystalized after the shear deformation. Generally, CPO patterns change with deformation conditions such as temperature, pressure and strain history (Passchier and Trouw, 1996). The difference of antigorite CPO may depend on such factors, but with the samples presented here we cannot come up with conclusions. Clearly more studies are needed to understand the difference between the two antigorite fabric patterns.

5.3. Anisotropy of elastic properties

Based on CPO and single crystal elastic constants for antigorite (Bezacier et al., 2010, their Table 2) elastic properties of the serpentinites B and C were calculated using a self-consistent method that takes particle shapes into account (Matthies, 2012; Vasin et al., 2013). Stiffness tensors based on X-ray data for serpentinites B and C are listed in Table 2 and compared with single crystal values. From stiffness tensors P-wave velocities and shear-wave splitting surfaces were calculated, assuming a density of 2.62 g/cm^3. Fig. 11 indicates similar patterns for serpentinites B and C, but B is more anisotropic, consistent with stronger preferred orientation. Slowest P-wave velocities (serpentinite B; 6.3 km/s and serpentinite C; 6.4 km/s) are perpendicular to the foliation and fastest velocities (7.4 and 7.1 km/s) parallel to the lineation. Shear-wave splitting is strongest in the foliation plane (0.6 and 0.4 km/s), with fast S-waves polarized parallel to foliation plane.

Table 3 is a list of P-wave velocities and anisotropies (AVp = 200 ∗ (Vpmax − Vpmin) / ((Vpmax + Vpmin))) and S-wave anisotropy (AVs max = 200 ∗ (Vs1 − Vs2) / ((Vs1 + Vs2))) of the direction with strongest shear-wave splitting (Pera et al., 2003) for different data sets. Interestingly, for serpentinite B P-wave anisotropies (AVp) are higher for synchrotron X-rays than for EBSD data. It does reflect the (001) pole partial girdle distribution, since the P-wave velocity of antigorite single crystals is at a maximum in the [100] direction and a minimum in the [001] direction (Bezacier et al., 2010). Anisotropies in the three samples from this study are considerably lower than others reported in the literature (e.g. Bezacier et al., 2010, Hirauchi et al., 2010, Jung, 2011, Kern et al., 1997, Nishii et al., 2011). This illustrates the importance of large volume averages for deriving geophysically relevant averages. For this study even the X-ray measurements have been selective and an average over larger specimens in the cm-range, e.g. by neutron diffraction would no doubt produce weaker textures and thus predict weaker seismic anisotropy.

Seismic anisotropy in subduction zones has been the subject of recent discussions (e.g. Bezacier et al., 2010; Boudier et al., 2010; Christensen, 2004; Jung, 2011; Katayama et al., 2009; Mookherjee and Capitani, 2011; Watanabe et al., 2011). Compared with Bezacier et al.

Table 3
Maximum and minimum P-wave velocities (in km/s), P-wave anisotropy (AVp) (%), maximum shear-wave splitting (dVs max) (in km/s) and maximum S-wave anisotropy (AVs max) (%) for different samples. Hirauchi et al. (2010) is "schistose type" in their measurements. (1) Geometric averaging, (2) self-consistent, (3) Voigt–Reuss–Hill averaging, (4) experimental at 600 MPa, and (5) containing 80.2% antigorite and experimental at 180 MPa.

Sample	Vp max (km/s)	Vp min (km/s)	AVp (%)	dVs max (km/s)	AVs max (%)
Serpentinite A EBSD Fig. 6d (1)	7.41	6.10	19.4	0.80	21.3
Serpentinite B EBSD Fig. 10b (1)	7.15	6.35	11.9	0.67	18.3
Serpentinite B X-ray (2)	7.36	6.31	15.4	0.59	15.3
Serpentinite C X-ray (2)	7.14	6.42	10.6	0.39	10.2
Bezacier et al. (2010) (1)	8.47	5.73	38.6	2.04	53.7
Hirauchi et al. (2010) (3)	8.15	5.94	31.3	1.38	36.0
Jung (2011) (3)	7.70–8.12	5.92–6.08	23.6–31.4	–	22.8–36.5
Nishii et al. (2011) (3)	7.55–8.19	5.90–6.30	18.0–32.5	–	14.0–36.2
Kern et al. (1997) (4)	7.68	6.02	24.2	13.0	34.2
Watanabe et al. (2011) (5)	7.70	5.83	28	0.9	26
Ji et al. (2013) (4)	–	–	3.8–16.3	0.43–0.04	3.6–18.3

(2010), the maximum Vp direction is different from our study. Their highest Vp is perpendicular to the lineation in the foliation, reflecting the CPO patterns of antigorite. Recalculating their Table 3 with a geometric mean, the anisotropies of their results are higher, AVp; 38.6% and maximum AVs; 53.7%, than this study (AVp; 10.6, 15.4%, AVs; 10.2, 15.3%). Other studies of foliated antigorite rich serpentinite also suggest higher elastic anisotropy (Vp; 31.3%, AVs; 36.0% in Hirauchi et al., 2010, Vp; 23.6–31.4%, AVs; 22.8–36.5% in Jung, 2011, Vp; 18.0–32.5%, AVs; 14.0–36.2%; in Nishii et al., 2011) (Table 3). The strong predicted anisotropies may be exaggerated and due to CPO measurements that emphasize a few well-oriented crystals. Elastic anisotropy of antigorite–olivine aggregates gives a weaker anisotropy than olivine free antigorite serpentinite (Jung, 2011; Wallis et al., 2011; Watanabe et al., 2011). Vp and Vs anisotropy values from experimental studies are in a similar range (Kern et al., 1997; Watanabe et al., 2011; Ji et al., 2013, Table 3). In this context the general significance of serpentinite for upper mantle anisotropy based on EBSD measurements should be evaluated.

Shear-wave anisotropy with trench-parallel fast propagation is observed in some subduction zones such as the Ryukyu arc and Tonga. Their splitting times range from 0.25 to 2 s (Long and Silver, 2008; Long and van der Hilst, 2006). The thickness (T) of an anisotropic layer is given by following equation (e.g., Pera et al., 2003); T = (100dt<Vs>) / AVs, where dt is delay time of the S-wave, <Vs> the average velocity, and AVs the anisotropy of S-waves (Fig. 12). This anisotropy has been attributed to an antigorite serpentinite layer above the subducting oceanic plate (e.g., Jung, 2011; Katayama et al., 2009; Mookherjee and Capitani, 2011). Compared with experimentally deformed olivine aggregate (Katayama et al., 2009; Zhang and Karato, 1995) which would require a slab thickness of 200–120 km for a delay time of 2 s, experimentally deformed serpentinite suggests a thickness of only 10–20 km (Katayama et al., 2009). For our natural samples the corresponding thickness is 50 km for serpentinite B, and 75 km for serpentinite C which is intermediate between experimental olivine and serpentine aggregates (Fig. 12).

Antigorite serpentinites with penetrative foliation, such as serpentinite mylonite and schists discussed here, are reported in several regions such as the Josephine ophiolite of California (Norrell et al., 1989), the Voltri-Massif and Zermatt-Saas Zone of the Western Alps (Hermann et al., 2000; Vogler, 1987; Wassmann et al., 2011). However, highly foliated serpentinite schists are rather localized and exceptional. For example are the occurrences in the California Coast Ranges and foothills of the Sierra Nevada (e.g. Andreani et al., 2005; Hirauchi et al., 2008; Wakabayashi, 2004) and the majority of serpentinites in the Central Alps, including Val Malenco (e.g. Molli, 1996; Tricart and Lemoine, 1983) where serpentinite is massive, without significant preferred orientation. The volume of the foliated antigorite serpentinite is important for interpreting the seismic anisotropy in a subduction zone.

6. Conclusions

Antigorite and olivine CPOs were measured to understand the fabric patterns and elastic properties of foliated antigorite serpentinites. We summarize the results of this study below, based on microstructural observations and comparisons between measured antigorite and olivine CPO patterns from three types of foliated antigorite serpentinite.

(1) Antigorite CPO patterns show (010) pole parallel to the lineation; and (001) pole normal to the foliation and partial girdle about the lineation. And this antigorite CPO pattern is directly formed from peridotite.
(2) At the thin section scale, the topotactic relationship does not explain the antigorite CPO that originated from the olivine CPO; i.e., it did not originate from B-type olivine in the host peridotite. Topotactic relationships should be erased during shear deformation.
(3) The three different measurement methods, U-stage, EBSD and Synchrotron X-ray, give qualitatively similar antigorite fabric patterns.
(4) In the subduction zone mantle wedge, the antigorite CPO has (010) pole parallel to the subduction direction and (001) pole normal to the subducting oceanic plate.
(5) CPOs from X-ray synchrotron predict similar elastic velocity geometry as those from EBSD measurements. However, it emphasizes the need to average over large sample volumes to obtain geophysically relevant physical properties.

Acknowledgments

We are grateful to Prof. Y. Saka (deceased 2011), Dr. T. Ohta, Mr. Y. Handa, and Mr. K. Okazaki (Waseda Univ.) for providing samples from the Toba area, Dr. I. Katayama (Hiroshima Univ.) for samples from the Nagasaki area and Prof. S. Wallis (Nagaoya Univ.) for the program of converting U-stage data to Euler angles. Y.S. is grateful to Prof. S. Arai, Prof. S. Umino, Prof. Morishita and Dr. Mizukami (Kanazawa Univ.) for the opportunity to visit the University of California, Berkeley. This work was supported by the "Institutional Program for Young Researcher Overseas Visits", part of the Japan Society for the Promotion of Science (Project heads at Kanazawa Univ.: Prof. Arai). HRW acknowledges support from NSF (EAR-0836402) and DOE (DE-FG02-05ER15637). We are appreciative for access to the BESSRC beamline 11 ID-C at APS of Argonne National Laboratory and to W. Kanitpanyacharoen and C. Benmore for help with the experiments. We appreciate comments by the editor (Prof. Jolivet) and two reviewers which helped us to improve the manuscript.

References

Andreani, M., Boullier, A.-M., Gratier, J.-P., 2005. Development of schistosity by dissolution–crystallization in a Californian serpentinite gouge. J. Struct. Geol. 27, 2256–2267.
Artioli, G., Rinaldi, R., Wilson, C.C., Zanazzi, P.F., 1995. High-temperature Fe–Mg cation partitioning in olivine; in-situ single-crystal neutron diffraction study. Am. Mineral. 80, 197–200.
Auzende, A.L., Guillot, S., Devouard, B., Baronnet, A., 2006. Serpentinites in an Alpine convergent setting: effects of metamorphic grade and deformation on microstructures. Eur. J. Mineral. 18, 21–33.
Bezacier, L., Reynard, B., Bass, J.D., Sanchez-Valle, G., Van de Moortèle, B., 2010. Elasticity of antigorite, seismic detection of serpentinites, and anisotropy in subduction zones. Earth Planet. Sci. Lett. 289, 198–208.
Bostock, M.G., Hyndman, R.D., Rondenay, S., Peacock, S.M., 2002. An inverted continental Moho and serpentinization of the forearc mantle. Nature 417, 536–538.
Boudier, F., Baronnet, A., Mainprice, D., 2010. Serpentine mineral replacements of natural olivine and their seismic implications: oceanic lizardite versus subduction-related antigorite. J. Petrol. 51, 495–512.
Chernak, L.J., Hirth, G., 2010. Deformation of antigorite serpentinite at high temperature and pressure. Earth Planet. Sci. Lett. 296, 23–33.
Christensen, N.I., 2004. Serpentinites, peridotites, and seismology. Int. Geol. Rev. 46, 795–816.
Deer, W.A., Howie, R.A., Zussman, J., 1992. An Introduction to the Rock-forming Minerals, 2nd ed. Longman, England.
Hawkes Jr., H.E., 1946. Olivine from Northern California showing perfect cleavage. Am. Mineral. 31, 276–283.
Hermann, J., Müntener, O., Scambelluri, M., 2000. The importance of serpentinite mylonites for subduction and exhumation of oceanic crust. Tectonophysics 327, 225–238.
Hilairet, N., Reynard, B., Wang, Y., Daniel, I., Merkel, S., Nishiyama, N., Petitgirard, S., 2007. High-pressure creep of serpentine, interseismic deformation, and initiation of subduction. Science 318, 1910–1913.
Hirauchi, K., Tamura, A., Arai, S., Yamaguchi, H., Hisada, K., 2008. Fertile abyssal peridotites within the Franciscan subduction complex, central California: possible origin as detached remnants of oceanic fracture zones located close to a slow-spreading ridge. Lithos 105, 319–328.
Hirauchi, K., Michibayashi, K., Ueda, H., Katayama, I., 2010. Spatial variations in antigorite fabric across a serpentinite subduction channel: insights from the Ohmachi Seamount, Izu–Bonin frontal arc. Earth Planet. Sci. Lett. 299, 196–206.
Hyndman, R.D., Peacock, S.M., 2003. Serpentinization of the forearc mantle. Earth Planet. Sci. Lett. 212, 417–432.
Ji, S., Li, A., Wang, Q., Long, C., Wang, H., Marcotte, D., Salisbury, M., 2013. Seismic velocities, anisotropy, and shear-wave splitting of antigorite serpentinites and tectonic implications for subduction zones. J. Geophys. Res. Solid Earth 118, 1015–1037.
Jung, H., 2011. Seismic anisotropy produced by serpentine in mantle wedge. Earth Planet. Sci. Lett. 307, 535–543.

Jung, H., Karato, S., 2001. Water-induced fabric transitions in olivine. Science 293, 1460–1463.
Jung, H., Katayama, I., Jiang, Z., Hiraga, T., Karato, S., 2006. Effect of water and stress on the lattice-preferred orientation of olivine. Tectonophysics 421, 1–22.
Katayama, I., Hirauchi, K., Michibayashi, K., Ando, J., 2009. Trench-parallel anisotropy produced by serpentine deformation in the hydrated mantle wedge. Nature 461, 1114–1117.
Kamb, W.B., 1961. The thermodynamic theory of nonhydrostatically stressed solids. J. Geophys. Res. 66, 259–271.
Kern, H., 1993. P- and S-wave anisotropy and shear-wave splitting at pressure and temperature in possible mantle rocks and their relation to the rock fabric. Phys. Earth Planet. Inter. 78, 245–256.
Kern, H., Liu, B., Popp, T., 1997. Relationship between anisotropy of P and S wave velocities and anisotropy of attenuation in serpentinite and amphibole. J. Geophys. Res. 102, 3051–3065.
Long, M.D., Silver, P.G., 2008. The subduction zone flow field from seismic anisotropy: a global view. Science 319, 315–318.
Long, M.D., van der Hilst, R.D., 2006. Shear wave splitting from local events beneath the Ryukyu arc: trench-parallel anisotropy in the mantle wedge. Phys. Earth Planet. Inter. 155, 300–312.
Lutterotti, L., Matthies, S., Wenk, H.-R., Schultz, A.S., Richardson, J.W., 1997. Combined texture and structure analysis of deformed limestone from time-of-flight neutron diffraction spectra. J. Appl. Phys. 81, 594–600.
Lutterotti, L., Vasin, R., Wenk, H.-R., 2013. Rietveld texture analysis from synchrotron diffraction images: I. Basic analysis. Powder Diffract. (in press).
Matthies, S., Wenk, H.-R., 2009. Transformations for monoclinic crystal symmetry in texture analysis. J. Appl. Crystallogr. 42, 564–571.
Matthies, S., 2012. GEO-MIX-SELF calculations of the elastic properties of a textured graphite sample at different hydrostatic pressures. J. Appl. Crystallogr. 45, 1–16.
Mizukami, T., Wallis, S.R., 2005. Structural and petrological constraints on the tectonic evolution of the garnet–lherzolite facies Higashi-akaishi peridotite body, Sanbagawa belt, SW Japan. Tectonics 24. http://dx.doi.org/10.1029/2004TC001733 TC6012.
Molli, G., 1996. Pre-orogenic tectonic framework of the Northern Apennine ophiolites. Eclogae Geol. Helv. 89, 163–180.
Mookherjee, M., Capitani, G.C., 2011. Trench parallel anisotropy and large delay times: elasticity and anisotropy of antigorite at high pressures. Geophys. Res. Lett. 38. http://dx.doi.org/10.1029/2011GL047160 L09315.
Morales, L.F.G., Mainprice, D., Boudier, F., 2013. The influence of hydrous phase on the microstructure and seismic properties of a hydrated mantle rock. Tectonophysics 594, 103–117.
Nagasaki City, 2013. Geological map of Nagasaki City. Accompanying map in the History of Nagasaki City. (in Japanese).
Norrell, G.T., Teixell, A., Harper, G.D., 1989. Microstructure of serpentinite mylonites from the Josephine ophiolite and serpentinization in retrogressive shear zones, California. Geol. Soc. Am. Bull. 101, 673–682.
Nishii, A., Wallis, S.R., Mizukami, T., Michibayashi, K., 2011. Subduction related antigorite CPO patterns from forearc mantle in the Sanbagawa belt, southwest Japan. J. Struct. Geol. 33, 1436–1445.
Nishimura, Y., 1998. Geotectonic subdivision and areal extent of the Sangun belt, Inner Zone of Southwest Japan. J. Metamorph. Geol. 16, 129–140.
Nishiyama, T., 1990. CO2-metasomatism of a metabasite block in a serpentine melange from the Nishisonogi metamorphic rocks, southwest Japan. Contrib. Mineral. Petrol. 104, 35–46.
Nozaka, T., 2005. Metamorphic history of serpentinite mylonites from the Happo ultramafic complex, central Japan. J. Metamorph. Geol. 23, 711–723.
Nozaka, T., Ito, Y., 2011. Cleavable olivine in serpentinite mylonite from the Oeyama ophiolite. J. Mineral. Petrol. Sci. 106, 36–50.
Padrón-Navarta, J.A., Tommasi, A., Garrido, C.J., López Sánchez-Vizcaíno, V., 2012. Plastic deformation and development of antigorite crystal preferred orientation in high-pressure serpentinites. Earth Planet. Sci. Lett. 349–350, 75–86.
Passchier, C.W., Trouw, R.A.T., 1996. Microtectonics. Springer, Berlin.
Peacock, S.M., Hyndman, R.D., 1999. Hydrous minerals in the mantle wedge and the maximum depth of subduction thrust earthquakes. Geophys. Res. Lett. 26, 2517–2520.
Pera, E., Mainprice, D., Burlini, L., 2003. Anisotropic seismic properties of the upper mantle beneath the Torre Alfina area (Northern Apennines, Central Italy. Tectonophysics 370, 11–30.
Plümper, O., King, H.E., Vollmer, C., Ramasse, Q., Jung, H., Austrheim, H., 2012. The legacy of crystal–plastic deformation in olivine: high-diffusivity pathways during serpentinization. Contrib. Mineral. Petrol. 163, 701–724.
Saka, Y., Tezuka, S., Okada, Y.i, Ichikawa, M., Takagi, H., 1988. Gokasho–Arashima Tectonic Line, as a serpentinite melange zone, in the Shima Peninsula, Southwest Japan. J. Geol. Soc. Jpn. 94, 19–34 (Japanese and English abstract).
Shigeno, H., Mori, Y., Shimada, K., Nishiyama, T., 2012. Jadeities with metasomatic zoning from the Nishisonogi metamorphic rocks, western Japan: fluid-tectonic block interaction during exhumation. Eur. J. Mineral. 24, 289–311.
Shimizu, I., 1992. Nonhydrostatic and nonequilibrium thermodynamics of deformable materials. J. Geophys. Res. 97 (B4), 4587–4597.
Soda, Y., Takagi, H., 2010. Sequential deformation from serpentinite mylonite to metasomatic rocks along the Sashu Fault, SW Japan. J. Struct. Geol. 32, 792–802.
Teraoka, Y., Miyazaki, K., Hoshizumi, H., Yoshioka, T., Sakai, A., Ono, K., 1992. Geology of the Inukai district (with geological sheet map at 1:50,000). Geological Survey of Japan (in Japanese with English abstract).
Tricart, P., Lemoine, M., 1983. Serpentinite oceanic bottom in south Queyras ophiolites (French western Alps): record of the incipient oceanic opening of the Mesozoic Ligurian Tethys. Eclogae Geol. Helv. 76, 611–629.
Uehara, S., 1998. TEM and XRD study of antigorite superstructures. Can. Mineral. 36, 1595–1605.
Van de Moortèle, B., Bezacier, L., Trullenque, G., Reynard, B., 2010. Electron backscattering diffraction (EBSD) measurements of antigorite lattice-preferred orientations (LPO). J. Microsc. 239, 245–248.
Vasin, R., Wenk, H.-R., Kanitpanyacharoen, W., Matthies, S., Wirth, R., 2013. Anisotropy of Kimmeridge shale. J. Geophys. Res. 118, 1–26. http://dx.doi.org/10.1002/jgrb.50259.
Vogler, W.S., 1987. Fabric development in a fragment of Tethyan oceanic lithosphere from the Piemonte ophiolite nappe of the Western Alps, Valtournanche, Italy. J. Struct. Geol. 9, 935–953.
Wakabayashi, J., 2004. Contrasting setting of serpentinite bodies, San Francisco Bay Area, California: derivation from the subducting plate vs. Mantle Hanging Wall? Int. Geol. Rev. 46, 1103–1118.
Wallis, S.R., Kobayashi, H., Nishii, A., Mizukami, T., Seto, Y., 2011. Obliteration of olivine crystallographic preferred orientation patterns in subduction-related antigorite-bearing mantle peridotite: an example from the Higashi-Akaishi body, SW Japan. In: Prior, D.J., Rutter, E.H., Tatham, D.J. (Eds.), Deformation Mechanisms, Rheology and Tectonics: Microstructures, Mechanics and Anisotropy. Geological Society Special Publication, 360, pp. 113–127.
Wassmann, S., Stöckhert, B., Trepmann, C.A., 2011. Dissolution precipitation creep versus crystalline plasticity in high-pressure metamorphic serpentinites. In: Prior, D.J., Rutter, E.H., Tatham, D.J. (Eds.), Deformation Mechanisms, Rheology and Tectonics: Microstructures, mechanics and Anisotropy. Geological Society Special Publication, 360, pp. 129–149.
Watanabe, T., Kasami, H., Ohshima, S., 2007. Compressional and shear wave velocities of serpentinized peridotites up to 200 MPa. Earth Planets Space 59, 233–244.
Watanabe, T., Shirasugi, Y., Yano, H., Michibayashi, K., 2011. Seismic velocity in antigorite-bearing serpentinite mylonites. In: Prior, D.J., Rutter, E.H., Tatham, D.J. (Eds.), Deformation Mechanisms, Rheology and Tectonics: Microstructures, Mechanics and Anisotropy. Geological Society Special Publication, 360, pp. 97–112.
Wenk, H.-R., 1985. Measurement of pole figures. In: Wenk, H.-R. (Ed.), Preferred Orientation in Deformed Metals and Rocks: an Introduction to Modern Texture Analysis. Academic Press, Orlando, pp. 11–47.
Wenk, H.-R., Matthies, S., Donovan, J., Chateigner, D., 1998. BEARTEX, a Windows-based program system for quantitative analysis. J. Appl. Crystallogr. 31, 262–269.
Wenk, H.-R., Voltolini, M., Mazurek, M., Van Loon, L.R., Vinsot, A., 2008. Preferred orientations and anisotropy in shales: Callovo–Oxfordian shale (France) and Opalinus clay (Switzerland). Clay Clay Miner. 56, 285–306.
Wenk, H.-R., Kanitpanyacharoen, W., Voltolini, M., 2010. Preferred orientation of phyllosilicates: comparison of fault gouge, shale and schist. J. Struct. Geol. 32, 478–489.
Yokoyama, K., 1987. Ultramafic rocks in the Kurosegawa tectonic zone, Southwest Japan. J. Jpn. Assoc.Mineral. Petrol. Econ. Geol. 82, 319–335.
Zhang, S., Karato, S., 1995. Lattice preferred orientation of olivine aggregates deformed in simple shear. Nature 375, 774–777.